

Spin orbit coupling controlled spin pumping effect

L. Ma,¹ H. A. Zhou,² L. Wang,³ X. L. Fan,² W. J. Fan,¹
 D. S. Xue,² K. Xia,³ G. Y. Guo,^{4,5} and S. M. Zhou¹

¹*Shanghai Key Laboratory of Special Artificial Microstructure Materials and Technology and Pohl Institute of Solid State Physics and School of Physics Science and Engineering, Tongji University, Shanghai 200092, China*

²*The Key Lab for Magnetism and Magnetic Materials of Ministry of Education, Lanzhou University, Lanzhou 730000, People's Republic of China*

³*Department of Physics, Beijing Normal University, Beijing 100875, China*

⁴*Department of Physics, National Taiwan University, Taipei 10617, Taiwan*

⁵*Physics Division, National Center for Theoretical Sciences, Hsinchu 30013, Taiwan*

(Dated: December 7, 2024)

Abstract

Effective spin mixing conductance (ESMC) across the nonmagnetic metal (NM)/ferromagnet interface, spin Hall conductivity (SHC) and spin diffusion length (SDL) in the NM layer govern the functionality and performance of pure spin current devices with spin pumping technique. We show that all three parameters can be tuned significantly by the spin orbit coupling (SOC) strength of the NM layer in systems consisting of ferromagnetic insulating $\text{Y}_3\text{Fe}_5\text{O}_{12}$ layer and metallic $\text{Pd}_{1-x}\text{Pt}_x$ layer. Surprisingly, the ESMC is observed to increase significantly with x changing from 0 to 1.0. The SHC in PdPt alloys, dominated by the intrinsic term, is enhanced notably with increasing x . Meanwhile, the SDL is found to decrease when Pd atoms are replaced by heavier Pt atoms, due to the SOC induced spin flip scattering. The capabilities of both spin current generation and spin charge conversion is largely heightened via the SOC. These findings highlight the multifold tuning effects of the SOC in developing the new generation of spintronic devices.

With the prominent advantage of negligible Joule heat, the spin current plays a central role in the next generation of spintronic devices^{1–3}. Functionality and performance of pure spin current devices strongly depend on the generation and detection approaches of spin current. Among various generation approaches^{4–6}, the spin pumping has been widely used^{6–9}, in which the spin current is produced in a heavy non-magnetic metallic (NM) layer when the magnetization precession of the neighboring ferromagnet (FM) layer is excited by the microwave magnetic field, as shown in Fig. 1(a). Among a variety of detection techniques^{4,10}, the conventional electric approach is often employed to probe the spin current by means of inverse spin Hall effect (ISHE), where the spin current is converted into a charge current.

Since their original prediction^{11,12}, the spin Hall effect (SHE) and ISHE have become increasingly important because of their intriguing physics and great applications in the charge-spin conversion^{4,6,10,13–17}. It is commonly known that the SHE arises from the spin orbit coupling (SOC)¹⁷. As an outstanding issue, however, the qualitative dependence of the SHE on the SOC strength is still unclear. Moreover, the SHE is known to be contributed by the intrinsic, the skew scattering, and the side-jump terms^{17–22}. The issue of the SHE scaling law has not been understood yet although many attempts have been made. For instance, the intrinsic term has a dominant contribution to the spin Hall conductivity (SHC) in Ir doped Pt¹⁸ whereas the extrinsic skew scattering plays a major role in Ir doped Cu^{20–22}. In order to enhance the charge-spin conversion efficiency and to reveal the mechanism of the SHE, it is imperative to study the SHE in nonmagnetic alloys in which the SOC strength can be tuned continuously in a wide range.

The effective spin mixing conductance (ESMC) across the NM/FM interface has elicited a great deal of attention because it governs the spin pumping efficiency^{23–27}, i.e., the density of the dc spin current J_s as follows^{7,26}, $J_s = \frac{\hbar\omega}{4\pi} G_{mix}^{eff} \sin^2 \theta$, where G_{mix}^{eff} is the real part of the complex ESMC, the cone angle θ of the FM magnetization precession is determined by the ferromagnetic resonance (FMR) power absorption, $\omega = 2\pi f$ with the radio frequency f . It is appealing to reveal the physical mechanism of the ESMC because it is intimately related to the electronic band structure of the NM layer and chemical states on the surface of the FM layer^{23,24}. As well known, G_{mix}^{eff} is identified by the difference in the FMR full

width at half maximum (FWHM) between NM/FM and FM, $\Delta H_{NM/FM} - \Delta H_{FM}$ via the following equation⁷

$$G_{mix}^{eff} = \frac{4\pi\gamma M_s t_{FM}}{g\mu_B\omega} (\Delta H_{NM/FM} - \Delta H_{FM}), \quad (1)$$

where γ is the gyromagnetic ratio, g the Landé factor, t_{FM} the thickness of the FM layer, and M_s the magnetization of the FM layer. Since the change in the resonance linewidth of the FM layer is as small as a few oersteds after it is covered by a NM layer^{7,9,23-27}, much caution must be taken in order to accurately evaluate the magnitude of G_{mix}^{eff} .

As a critical parameter in spintronic devices, the spin diffusion length (SDL, λ_{sd}) controls the propagation of the spin current in the NM layer, leading to strong dependence of the ISHE voltage on the NM layer thickness. The mechanism of the SDL is in sharp debate although it has been studied extensively in both experiments and theory. For example, values of λ_{sd} in Pt measured by various research groups are not consistent^{16,19,28,29}, which is suggested to arise from different measurement approaches³⁰. In particular, although the SDL in heavy element NM layers such as Pt is assumed to arise from the spin flip scattering which is in turn caused by the SOC, the dependence of the SDL on the SOC strength is still an open question³¹.

The objective of this work is to study the ESMC, the SHE, and the SDL as a function of the SOC strength by implementing the $Pd_{1-x}Pt_x$ (PdPt)/ $Y_3Fe_5O_{12}$ (YIG) heterostructures, where the SOC can be tuned significantly whereas other physical properties are almost fixed. The SHC and in particular the ESMC are significantly enhanced via changing x from 0 to 1.0. Meanwhile, the SDL decreases with increasing x . These phenomena can be attributed to the SOC tuning effects. It will provide novel means to enhance the spin pumping efficiency and to improve the performance of spintronic devices. This work will also be helpful for the community in the newly emerging research field, i.e., the spin-orbitronics³².

First, we study the effect of the SOC on the ESMC. FMR spectra of YIG and Pt/YIG at $f = 9.0$ GHz in Fig. 1(b) can be described by Lorentz function⁷. In order to rigorously obtain the ESMC, the in-plane angular dependent FMR spectra of YIG and NM/YIG were measured. Interestingly, the resonance field and the linewidth both depend on the

orientation of the in-plane H , as shown in Figs. 1(c) and 1(d). The angular dependencies of the resonance field in YIG and Pt/YIG can be fitted by considering the in-plane uniaxial anisotropy³³ and the anisotropy energy is evaluated to be about 340 erg/cm³, much smaller than that of sputtered epitaxial YIG films on Gd₃Ga₅O₁₂ (GGG) substrates³⁴. The weak magnetic anisotropy indicates the strain relaxation of the YIG films. With the measured frequency dependence of the resonance magnetic field³³, $t_{FM} = 80$ nm, and $M_S = 136$ emu/cm³, the gyromagnetic ratio γ and the Landé factor g are fitted to be 17.57 GHz/kOe and 2.0, respectively. Here, the accuracy of $\Delta H_{NM/FM}$ and ΔH_{FM} in Eq. 1 is significantly enhanced by averaging the data points at all orientations. The linewidth enhancement in Pt/YIG arises from the energy transfer from the YIG to the NM layers when the spin angular momentum passes the interface during the spin pumping⁷. Surprisingly, G_{mix}^{eff} increases with increasing x , as shown in Fig. 1(e). For the present Pt/YIG, G_{mix}^{eff} is 7.9×10^{18} m⁻², close to the results (6.9×10^{18} m⁻²) of Wang *et al.*¹⁶. As pointed out by Tserkovnyak and Jiao *et al.*³⁵⁻³⁷, when λ_{sd} is significantly smaller than the NM layer thickness, the real part of the ESMC at the FM/FM interface is modified by the NM layer thickness and has a relationship with that of the spin mixing conductance (SMC) $G_{\uparrow\downarrow}$ as follows, $1/G_{mix}^{eff} = 1/G_{\uparrow\downarrow} + 1/A$ with the parameter $A = \sigma_{NM}/2\lambda_{sd}$ in the unit of h/e^2 . Accordingly, the real part of the SMC, $G_{\uparrow\downarrow}$ at the interface is achieved to be slightly larger than the G_{mix}^{eff} , as shown in Fig. 1(e).

In order to get better understanding of G_{mix}^{eff} , *ab initio* calculations were performed with and without the SOC³³, as shown in Fig. 1(f). Calculations show that G_{mix}^{eff} is enhanced by the SOC and increases monotonically with x . Since G_{mix}^{eff} changes little with T , the calculated results reproduce the measured data very well⁹. For a system without SOC, the G_{mix}^{eff} is governed by the number of channels available in the normal metal, which is hard to be changed. The SOC provides additional channels for the spin loss, leading to the G_{mix}^{eff} enhancement, which will open a new way to increase the spin pumping through interface. Surprisingly, one can expect even larger ESMC in samples with atomic flat Pt/YIG interface, as demonstrated by the fact that the calculated G_{mix}^{eff} value is twice larger than the measured one. Moreover, the difference between the calculated and measured results in Pd/YIG is much larger than that of Pt/YIG. This phenomenon might come from the better film quality of Pt, as evidenced by the scenario that the Pt layer has a lower

resistivity as shown below although bulk Pt and Pd have identical resistivity. Therefore, the SOC tuning effect on G_{mix}^{eff} may strongly depend on the microstructure of the NM layer, in addition to the morphology and chemical state on the surface of the YIG³⁸.

We now consider the effect of the SOC on the SDL in the NM layer. With the sensing charge current along the x axis in the film plane as shown in the inset of Fig. 2, the NM/YIG exhibits spin Hall magnetoresistance(SMR) effect^{39,40} and the sheet longitudinal resistivity obeys the following equation $\rho_{xx} - \rho_0 = \Delta\rho m_y^2$, where m_y is the y component of the magnetization unit vector in the YIG layer. As the external magnetic field is rotated in the yz plane, the ρ_{xx} changes as a scale of $\cos^2 \theta_H$, as observed in Pt/YIG bilayers in Fig. 2(a). The $\Delta\rho/\rho_0$ ratio changes non-monotonically with the NM layer thickness, as shown in Fig. 2(b). According to the SMR theory, the measured results in Fig.2(b)³³ are fitted and λ_{sd} is found to be 1.05 nm for Pt/YIG, which is highly close to the measured results (1.2 nm) of Zhang *et al*²⁸. Interestingly, λ_{sd} of PdPt alloys at room temperature is found to decrease with increasing x , as shown in Fig. 2(c). The measured x dependence can be fitted by $\lambda_{sd} = 3.616 - 7.31x + 6.85x^2 - 2.08x^3$, and accordingly the λ_{sd} can be obtained for all samples. The SOC strength ξ in PdPt alloys increases as a scale of $Z^{2.56}$ (Z =atomic number), as shown by the first-principles calculations in Fig. 2(d)³³. It is noted that $\lambda_{sd}(\text{Pt})/\lambda_{sd}(\text{Pd}) \simeq \xi(\text{Pd})/\xi(\text{Pt})$. Within the SOC induced spin flip scattering model³¹, the SDL should decrease with increasing ξ . The variation of λ_{sd} with x in Fig. 2(c) agrees with the spin flip scattering model⁴¹. Thus, the decay of pure spin current in PdPt alloys is mainly caused by the Elliot-Yafet spin flip scattering^{27,31}.

Then, we investigate the functional dependence of the SHE on the Pt atomic concentration. In experiments of the spin pumping, PdPt/YIG films were patterned into microstrips (2 mm in length, 20 μm in width) by using photolithography and ion etching. As shown in Fig. 3(a), those strips are placed in the slots between signal (S) and ground (G) of coplanar waveguide (Pt 100 nm) fabricated by sputtering and lift-off techniques. When an alternating current of $f = 10$ GHz is applied along the signal line, a radio frequency magnetic field h_z perpendicular to the film plane is induced to trigger the precession of the FM magnetization. V_{ISHE} between both ends of the strip sample along the x axis was detected as a function of H . Figure 3(b) shows typical V_{ISHE} as a function of H at $\alpha = -90$ degrees,

$f = 10$ GHz, and $P_{in} = 100$ mW for Pt/YIG sample. The maximal voltage is detected at $H_{RES} = 2.56$ kOe, the resonance field of the YIG layer. The symmetrical Lorentz line shape (in Fig. 3(b)) and the $\sin \alpha$ angular dependent amplitude as shown in supplementary materials³³ indicate the pure ISHE origin of the resonance voltage⁷. The inset in Fig. 3(b) shows that for Pt/YIG the measured V_{ISHE} increases with increasing P_{in} . At high P_{in} , the oscillations of the voltage on the high magnetic field side are caused by the excitation of spin waves⁴⁴. Figure 3(c) shows that for all samples the measured results slightly deviate from the linear dependence, possibly due to the occurrence of nonlinear multimagnon scattering channels⁴⁵. Figure 3(d) shows that V_{ISHE} changes non-monotonically with x and achieves a maximal value near $x = 0.7$. At $P_{in} = 120$ mW, the maximal V_{ISHE} is as large as $300 \mu V$. In the spin pumping technique, V_{ISHE} obeys the following equation⁷

$$V_{ISHE} = -\frac{eL\omega G_{mix}^{eff}\theta_{SH}\lambda_{sd}\rho}{2\pi t_{NM}} \tanh\left(\frac{t_{NM}}{2\lambda_{sd}}\right)\theta^2 \sin \alpha, \quad (2)$$

with the cone angle of the FM magnetization precession θ , $L = 2.0$ mm, $t_{NM} = 15$ nm, and the orientation of the magnetization $\alpha = -90$ degrees.

With V_{ISHE} in Fig. 3(d) and θ in supplementary materials³³ at $P_{in} = 20$ mW, and other parameters in Eq. 2, θ_{SH} of PdPt can be deduced for all x . In experiments³³, θ_{SH} is found to increase with increasing x . For instance, θ_{SH} is 0.045 and 0.125 for Pd and Pt, respectively. The measured value of the present Pt/YIG is close to the results of 0.12 reported by Zhang *et al.*³⁷. It is noted that the observed variation of θ_{SH} deviates from the Z^4 dependence¹⁶. Interestingly, the measured results are also confirmed by the SMR approach³³. For example, the value of θ_{SH} in Pt/YIG is fitted to be 0.120, in agreement with the results by the spin pumping technique.

Figures 4(a) and 4(b) summarize the results of σ_{SH} and ρ at 300 K, where $\sigma_{SH} = \theta_{SH}\sigma\hbar/e$ with the electric conductivity σ of the NM layer. The measured σ_{SH} increases monotonically with increasing x . σ_{SH} of about $2500 \hbar/e$ S/cm for Pt is enhanced significantly, compared with that of $665 \hbar/e$ S/cm for Pd. Interestingly, the measured SHC results of Pt/YIG and Pd/YIG are close to the intrinsic SHC with the first-principles relativistic band model, $2200 \hbar/e$ S/cm for Pt and $1300 \hbar/e$ S/cm for Pd⁴⁶, as shown in Fig. 4(a). For the NM layers, the non-monotonic change of ρ in Fig. 4(b) indicates the random location of the Pd and Pt atoms and the formation of single phase solid solution in PdPt layers⁴⁷.

Ab initio calculations based on the scattering model show that σ_{SH} and ρ at 0 K both exhibit non-monotonic variation trends with x , as shown in Figs. 4(c) and 4(d). The calculated SHC within the scattering model should consist of the intrinsic and extrinsic terms for x in the region from 0 to 1.0. The extrinsic one, caused by the asymmetric scattering at impurity sites, is negligible near the ending data points^{18,46} and becomes prominent near $x = 0.5$, as proved by similar variation trends of the SHC and the resistivity. However, it should be pointed out that the measured results for intermediate x in Fig. 4(a) cannot be explained in terms of the scattering model. The discrepancy between measured and calculated results might be caused by the fact that neither the short range ordering⁴⁷, nor defects, nor grain boundaries is considered in calculations²². Moreover, the divergence may also come from the different temperature dependencies of the intrinsic term and the extrinsic one. Clearly, for the present PdPt alloys, the intrinsic term plays a dominant role in the measured SHC and the extrinsic term can be neglected, as observed in Ir doped Pt¹⁸. It is the predominant contribution of the intrinsic term that leads to the weak dependence of the spin Hall angle on the NM layer thickness. Indeed, in the analysis of the SDL in PdPt alloys, the measured SMR results in Fig. 2(b) can be well fitted assuming the spin Hall angle is independent of the NM layer thickness⁴⁰. As one of major issues in this field^{17–22}, the mechanism of the extrinsic SHC needs further investigations.

To summarize, a unique heterostructure system consisting of isoelectronic PdPt alloy and YIG is employed to explore the mechanism of the ESMC, the SHE, and the SDL. Among various physics parameters, only the SOC strength is tuned significantly by changing the alloy composition. The value of G_{mix}^{eff} is rigorously evaluated by measuring the angular dependent resonance linewidth in both YIG and PdPt/YIG. Surprisingly, G_{mix}^{eff} is found to increase when the Pd atoms are replaced by heavier Pt atoms. *Ab initio* calculations clearly show that the G_{mix}^{eff} enhancement stems from an increasing SOC strength. It is found that σ_{SH} increases with increasing x thanks to the dominant intrinsic contribution. At the same time, the SDL decreases with increasing x , indicating the validity of the spin-flip scattering model in PdPt alloys.

For PdPt/YIG, the generation efficiency of spin current density J_s is enhanced signif-

icantly when x changes from 0 to 1.0. For Pt/YIG, J_s is larger than that of Pd/YIG by a factor of 7. The J_s enhancement will make it easier for the spin current to drive both the magnetization switching and the domain wall motion. Furthermore, the conversion efficiency between the spin current and the charge current in Pt/YIG is larger than that of Pd/YIG by a factor of 2. This offers control over the generation/detection efficiency of spin current and favors to reduce the charge current threshold in spin transfer torque induced magnetization switching. In a word, these findings presented here provide multiple degrees of freedom for improving the functional performance of state-of-the-art spintronic devices and will also provoke further theoretical investigation of the spin dependent transport properties in the NM layers.

I. METHODS

Sample description. A series of heretostructures consisting of 80 nm thick YIG single-crystal films and PdPt alloy layer were fabricated on (111)-oriented single crystalline $\text{Gd}_3\text{Ga}_5\text{O}_{12}$ (GGG) substrates via pulsed laser deposition and subsequent DC magnetron sputtering.

Experimental method. The film thickness and microstructure were characterized by x-ray reflection (XRR) and x-ray diffraction (XRD). Magnetization hysteresis loops were measured by physical property measurement system (PPMS). The ISHE voltage V_{ISHE} was detected by spin pumping technique, in combination of the FMR technique. The resonance linewidths of YIG and PdPt/YIG were measured by the FMR technique with in-plane H . The SDL was measured by the spin Hall magnetoresistance (SMR) technique⁴⁰. Details of fabrication and measurements are described in supplementary materials³³.

***Ab initio* calculations for ESMC and SHC.** The atomic potentials of the PdPt/YIG interface were obtained with the tight-binding linear-muffin-tin-orbital method in the augmented spherical wave approximation. Details of calculations of the ESMC, SHC, and SOC strength are described in supplementary materials³³.

¹ Jungwirth, T., Wunderlich, J., and Olejnik, K. Spin Hall effect devices. *Nat. Mater.* **11**, 382-390(2012)

² Liu, L., Lee, O. J., Gudmundsen, T. J., Ralph, D. C., and Buhrman, R. A. Current-Induced Switching of Perpendicularly Magnetized Magnetic Layers Using Spin Torque from the Spin Hall Effect. *Phys. Rev. Lett.* **109**, 096602(2012)

³ Miron, I. M., Moore, T., Szambolics, H., Buda-Prejbeanu, S., Auffret, L. D., Rodmacq, B., Pizzini, S., Vogel, J., Bonfim, M., Schuhl, A., and Gaudin, G. Fast current-induced domain-wall motion controlled by the Rashba effect, *Nat. Mater.* **10**, 419(2011).

⁴ Kato, Y. K., Myers, R. C., Gossard, A. C., and Awschalom, D. D. Observation of the Spin Hall Effect in Semiconductors. *Science* **306**, 1910(2004)

⁵ Uchida, K., Takahashi, S., Harii, K., Ieda, J., Koshiba, W., Ando, K., Maekawa, S., and Saitoh, E. Observation of the spin Seebeck effect, *Nature* **455**, 778-781 (2008)

⁶ Costache, M. V., Sladkov, M., Watts, S. M., Wal, C. H. van der., and Wees, B. J. van. Electrical Detection of Spin Pumping due to the Precessing Magnetization of a Single Ferromagnet. *Phys. Rev. Lett.* **97**, 216603(2006)

⁷ Mosendz, O., Pearson, J. E., Fradin, F. Y., Bauer, G. E. W., Bader, S. D., and Hoffmann, A. Quantifying Spin Hall Angles from Spin Pumping: Experiments and Theory. *Phys. Rev. Lett.* **104**, 046601(2010)

⁸ Hahn, C., Loubens, G. de, Viret, M., Klein, O., Naletov, V. V., and Youssef, J. B. Detection of Microwave Spin Pumping Using the Inverse Spin Hall Effect. *Phys. Rev. Lett.* **111**, 217204(2013)

⁹ Czeschka, F. D., Dreher, L., Brandt, M. S., Weiler, M., Althammer, M., Imort, I. M., Reiss, G., Thomas, A., Schoch, W., Limmer, W., Huebl, H., Gross, R., and Goennenwein, S. T. B. Scaling Behavior of the Spin Pumping Effect in Ferromagnet-Platinum Bilayers. *Phys. Rev. Lett.* **107**, 046601(2011)

¹⁰ Valenzuela, S. O. and Tinkham, M. Direct electronic measurement of the spin Hall effect. *Nature (London)* **442**, 176(2006)

¹¹ Dyakonov, M., and Perel, V. I. Possibility of Orienting Electron Spins with Current. *Sov. Phys. JETP Lett.* **13**, 467-469(1971)

¹² Dyakonov, M., and Perel, V. I. Current-induced spin orientation of electrons in semiconductors. *Phys. Lett. A* **35**, 459(1971)

¹³ Hirsch, J. E. Spin Hall Effect. *Phys. Rev. Lett.* **83**, 1834(1999)

¹⁴ Zhang, S. Spin Hall Effect in the Presence of Spin Diffusion. *Phys. Rev. Lett.* **85**, 393(2000)

¹⁵ Saitoh, E., Ueda, M., Miyajima, H., and Tatara, G. Conversion of spin current into charge current at room temperature: Inverse spin-Hall effect. *Appl. Phys. Lett.* **88**, 182509(2006)

¹⁶ Wang, H. L., Du, C. H., Pu, Y., Adur, R., Hammel, P. C., and Yang, F. Y. Scaling of Spin Hall Angle in 3d, 4d, and 5d Metals from $\text{Y}_3\text{Fe}_5\text{O}_{12}$ /Metal Spin Pumping. *Phys. Rev. Lett.* **112**, 197201(2014)

¹⁷ Hoffmann, A. Spin Hall effect in metals. *IEEE Trans. Magn.* **49**, 5172(2013)

¹⁸ Lowitzer, S., Gradhand, M., Ködderitzsch, D., Fedorov, D. V., Mertig, I., and Ebert, H., Extrinsic and Intrinsic Contributions to the Spin Hall Effect of Alloys. *Phys. Rev. Lett.* **106**, 056601 (2011)

¹⁹ Morota, M., Niimi, Y., Ohnishi, K., Wei, D. H., Tanaka, T., Kontani, H., Kimura, T., and Otani, Y. Indication of intrinsic spin Hall effect in 4d and 5d transition metals. *Phys. Rev. B* **83**, 174405 (2011)

²⁰ Gradhand, M., Fedorov, D. V., Zahn, P. and Mertig, I. Spin Hall angle versus spin diffusion length: Tailored by impurities. *Phys. Rev. B* **81**, 245109(2010)

²¹ Niimi, Y., Kawanishi, Y., Wei, D. H., Deranlot, C., Yang, H. X., Chshiev, M., Valet, T., Fert, A., and Otani, Y. Giant Spin Hall Effect Induced by Skew Scattering from Bismuth Impurities inside Thin Film CuBi Alloys. *Phys. Rev. Lett.* **109**, 156602(2012)

²² Fedorov, D. V., Herschbach, C., Johansson, A., Ostanin, S., Mertig, I., Gradhand, M., Chadova, K., Ködderitzsch, D., and Ebert, H. Analysis of the giant spin Hall effect in Cu(Bi) alloys. *Phys. Rev. B* **88**, 085116(2013)

²³ Xia, K., Kelly, P. J., Bauer, G. E. W., Brataas, A., and Turek, I. Spin torques in ferromagnetic/normal-metal structures. *Phys. Rev. B* **65**, 220401(2002)

²⁴ Carva, K. and Turek, I. Spin-mixing conductances of thin magnetic films from first principles. *Phys. Rev. B* **76**, 104409(2007)

²⁵ Jia, X., Liu, K., Xia, K. and Bauer, G. E. W. Spin transfer torque on magnetic insulators. *EPL (Europhysics Letters)* **96**, 17005 (2011)

²⁶ Weiler, M., Althammer, M., Schreier, M., Lotze, J., Pernpeintner, M., Meyer, S., Huebl, H.,

Gross, R., Kamra, A., Xiao, J., Chen, Y. T., Jiao, H. J., Bauer, G. E. W., and Goennenwein, S. T. B. Experimental Test of the Spin Mixing Interface Conductivity Concept. *Phys. Rev. Lett.* **111**, 176601(2013)

²⁷ Liu, Y., Yuan, Z., Wesselink, R. J. H., Starikov, A. A., and Kelly, P. J. Interface Enhancement of Gilbert Damping from First Principles. *Phys. Rev. Lett.* **113**, 207202(2014)

²⁸ Zhang, W., Vlaminck, V., Pearson, J. E., Divan, R., Bader, S. D., and Hoffmann, A., Determination of the Pt spin diffusion length by spin-pumping and spin Hall effect. *Appl. Phys. Lett.* **103**, 242414 (2013).

²⁹ Isasa, M., Villamor, E., Hueso, L. E., Gradhand, M., and Casanova, F. Temperature dependence of spin diffusion length and spin Hall angle in Au and Pt. *Phys. Rev. B* **91**, 024402 (2015)

³⁰ Chen, K. and Zhang, S. F. Spin Pumping in the Presence of Spin-Orbit Coupling. *Phys. Rev. Lett.* **114**, 126602 (2015)

³¹ Takahashi, S. and Maekawa, S. Spin current, spin accumulation and spin Hall effect. *Sci. Technol. Adv. Mater.* **9**, 014105(2008)

³² Manchon, A. Spin-orbitronics: A new moment for Berry. *Nat. Phys.* **10**, 340 (2014).

³³ See supplemental material for sample fabrication, measurements of XRR, XRD, magnetization hysteresis loops, FMR, SMR, and spin pumping, and *ab initio* calculations.

³⁴ Wang, H., Du, C., Hammel, P. C., and Yang, F. Y. Strain-tunable magnetocrystalline anisotropy in epitaxial $Y_3Fe_5O_{12}$ thin films. *Phys. Rev. B* **89** 134404(2014)

³⁵ Tserkovnyak, Y., Brataas, A., and Bauer, G. E. W. Spin pumping and magnetization dynamics in metallic multilayers. *Phys. Rev. B* **66**, 224403 (2002)

³⁶ Jiao, H. and Bauer, G. E. W. Spin backflow and ac voltage generation by spin pumping and the inverse spin Hall effect. *Phys. Rev. Lett.* **110**, 217602 (2013).

³⁷ Zhang, W. F., Han, W., Jiang, X., Yang, S. H., and Parkin, S. S. P. Role of transparency of platinum-ferromagnet interfaces in determining the intrinsic magnitude of the spin Hall effect, *Nat. Phys.* **11**, 496-502 (2015)

³⁸ Jungfleisch, M. B., Lauer, V., Neb, R., Chumak, A. V., and Hillebrands, B. Improvement of the yttrium iron garnet/platinum interface for spin pumping-based applications. *Appl. Phys. Lett.* **103**, 022411(2013)

³⁹ Nakayama, H., Althammer, M., Chen, Y. T., Uchida, K., Kajiwara, Y., Kikuchi, D., Ohtani, T., Geprägs, S., Opel, M., Takahashi, S., Gross, R., Bauer, G. E. W., Goennenwein, S. T. B., and

Saitoh, E. Spin Hall Magnetoresistance Induced by a Nonequilibrium Proximity Effect, *Phys. Rev. Lett.* **110**, 206601(2013)

⁴⁰ Althammer, M., Meyer, S., Nakayama, H., Schreier, M., Altmannshofer, S., Weiler, M., Huebl, H., Geprägs, S., Opel, M., Gross, R., Meier, D., Klewe, C., Kuschel, T., Schmalhorst, J. M., Reiss, G., Shen, L. M., Gupta, A., Chen, Y. T., Bauer, G. E. W., Saitoh, E., and Goennenwein, S. T. B. Quantitative study of the spin Hall magnetoresistance in ferromagnetic insulator/normal metal hybrids. *Phys. Rev. B* **87**, 224401(2013)

⁴¹ Marmion, S. R., Ali, M., McLaren, M., Williams, D. A., and Hickey, B. J. Temperature dependence of spin Hall magnetoresistance in thin YIG/Pt films, *Phys. Rev. B* **89**, 220404 (2014)

⁴² Kooten, J. J. van., Weller, G. A., and Ammerlaan, C. A. J. Electron paramagnetic resonance on iron-acceptor pairs in silicon. *Phys. Rev. B* **30**, 4564(1984)

⁴³ Hirst, L. L. Orbital angular momentum of 3d impurities in metals. *Z. Physik* **241**, 9(1971)

⁴⁴ Ando, K., Ieda, J., Sasage, K., Takahashi, S., Maekawa S., and Saitoh, E. Electric detection of spin wave resonance using inverse spin-Hall effect. *Appl. Phys. Lett.* **94**, 262505 (2009)

⁴⁵ Jungfleisch, M. B., Chumak, A. V., Kehlberger, A., Lauer, V., Kim, D. H., Onbasli, M. C., Ross, C. A., Kläui, M., and Hillebrands, B. Thickness and power dependence of the spin-pumping effect in $Y_3Fe_5O_{12}$ /Pt heterostructures measured by the inverse spin Hall effect. *Phys. Rev. B* **91**, 134407(2015)

⁴⁶ Guo, G. Y., Niu, Q., and Nagaosa, N. Anomalous Nernst and Hall effects in magnetized platinum and palladium. *Phys. Rev. B* **89**, 214406(2014)

⁴⁷ McGuire, T. R. and Potter, R. I. Anisotropic Magnetoresistance in Ferromagnetic 3d Alloys. *IEEE Trans. Magn.* **11**, 1018(1975)

II. ACKNOWLEDGEMENT

This work was supported by the State Key Project of Fundamental Research Grant No. 2015CB921501, the National Science Foundation of China Grant Nos. 11374227, 51331004, 51171129, and 51201114, Shanghai Science and Technology Committee Nos. 0252nm004, 13XD1403700, and 13520722700.

III. AUTHOR CONTRIBUTIONS

S. M. Z. and X. L. F. designed the experiments. L. M. fabricated the samples. L. M. and H. A. Z. carried out the measurements. L. W., K. X., and G. Y. G. performed the theory calculations. L. M., H. A. Z., X. L. F., W. J. F., D. S. X., L. W., and K. X. analyzed the data. L. M. and S. M. Z. wrote the paper and all the co-authors comment on it.

IV. ADDITIONAL INFORMATION

Supplementary information is available in the online version of the paper. Reprints and permissions information is available online at www.nature.com/reprints. Correspondence and requests for materials should be addressed to S. M. Z. and X. L. F.

V. COMPETING FINANCIAL INTERESTS

The authors declare no competing financial interests.

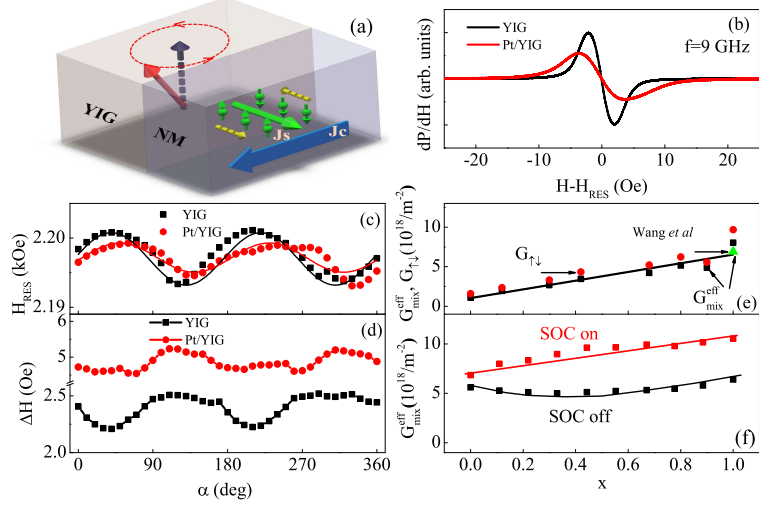


FIG. 1: Geometry of spin pumping (a). For 80 nm thick YIG and Pt(15 nm)/YIG(80 nm), typical FMR spectra (b), angular dependencies of the resonance field (c) and the resonance linewidth (d). Measured (e) and calculated (f) $G_{\text{mix}}^{\text{eff}}$. In (e), the measured data of Pt/YIG from Wang *et al* (blue triangle)¹⁶ and the SMC $G_{\uparrow\downarrow}$ (red circles) are given for comparison, and measurements were performed for PdPt(15 nm)/YIG(80 nm). Solid lines in (e, f) serve a guide to the eye. In (b, c, d, e), $T = 300$ K.

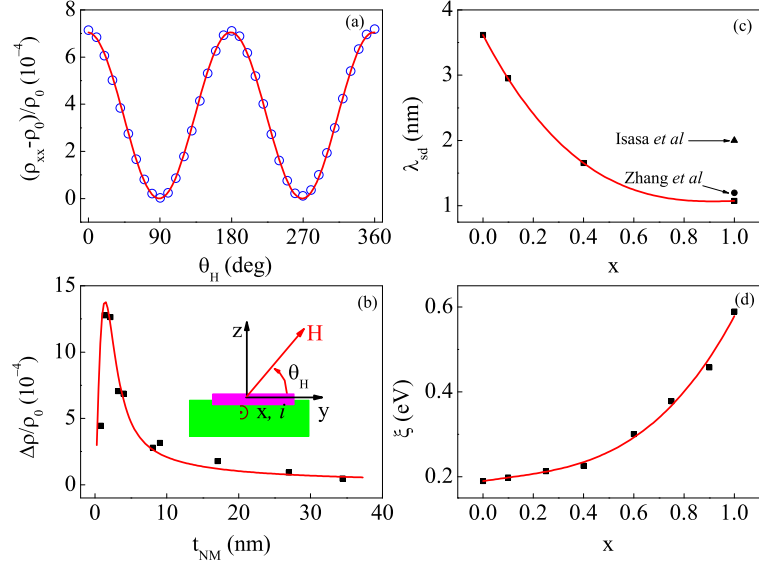


FIG. 2: For Pt(4 nm)/YIG(80 nm) bilayers, angular dependent SMR (a). For Pt/YIG (80 nm), dependence of the SMR ratio on the Pt layer thickness (b). Measured λ_{sd} in PdPt/YIG (80 nm) (c) and calculated ξ in PdPt alloys (d). Solid lines in (a, b, c, d) refer to the fitted results. In (c, d), the data were fitted in polynomials. In (c), the data of Pt provided by Zhang and Isasa *et al.*^{28,29} are also given for comparison. In (a, b), measurements were performed at room temperature.

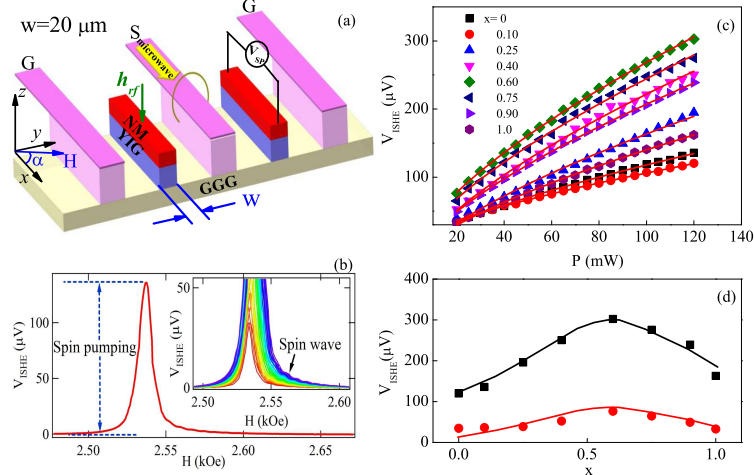


FIG. 3: (a) Measurement scheme of spin pumping technique. For Pt(15 nm)/YIG(80 nm) sample, V_{ISHE} with the sweeping H at $\alpha = -90$ degrees and an input microwave power $P_{in} = 100$ mW (b). For all PdPt(15 nm)/YIG(80 nm) samples, V_{ISHE} as a function of P_{in} (c), and V_{ISHE} versus x at $P_{in} = 20$ mW and 120 mW (d). In the inset of (b), P_{in} changes from 20 to 120 mW. Here, $T = 300$ K.

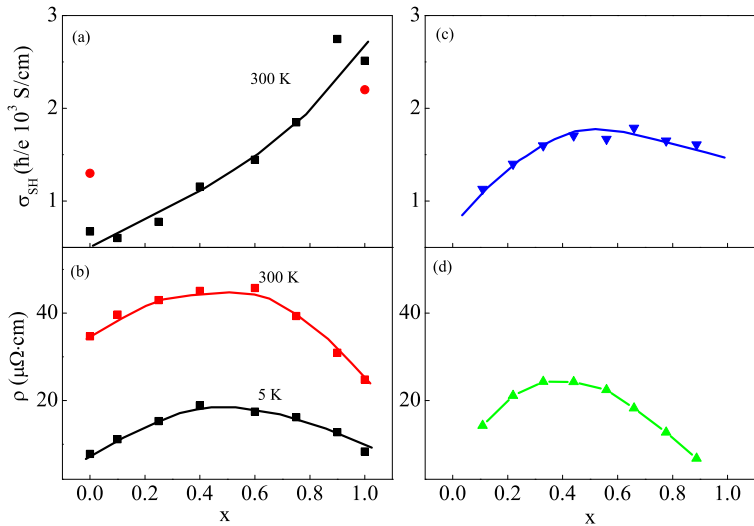


FIG. 4: Measured (a, b) and calculated (c, d) σ_{SH} (a, c) and resistivity (b, d) as a function of x . In (a), σ_{SH} was measured at 300 K. In (b), the resistivity was measured at 5 K and 300 K. In (a, b) measurements were performed for PdPt (15 nm)/YIG (80 nm). In (a) the intrinsic SHC of Pt and Pd are also given from the first-principles relativistic band model (red, solid circles)³³. In (c, d), the calculations are performed with the scattering model.